

SEDNet: Shallow Encoder-Decoder Network for Brain Tumor Segmentation

Chollette C. Olisah

School of Engineering,
University of the West of England, Bristol, UK.

Abstract

Despite the advancement in computational modeling towards brain tumor segmentation, of which several models have been developed, it is evident from the computational complexity of existing models which are still at an all-time high, that performance and efficiency under clinical application scenarios are limited. Therefore, this paper proposes a shallow encoder and decoder network named SEDNet for brain tumor segmentation. The proposed network is adapted from the U-Net structure. Though brain tumors do not assume complex structures like the task the traditional U-Net was designed for, their variance in appearance, shape, and ambiguity of boundaries makes it a compelling complex task to solve. SEDNet architecture design is inspired by the localized nature of brain tumors in brain images, thus consists of sufficient hierarchical convolutional blocks in the encoding pathway capable of learning the intrinsic features of brain tumors in brain slices, and a decoding pathway with selective skip path sufficient for capturing miniature local-level spatial features alongside the global-level features of brain tumor. SEDNet with the integration of the proposed preprocessing algorithm and optimization function on the BraTS2020 set reserved for testing achieves impressive dice and Hausdorff scores of 0.9308, 0.9451, 0.9026, and 0.7040, 1.2866, 0.7762 for non-enhancing tumor core (NTC), peritumoral edema (ED), and enhancing tumor (ET), respectively. Furthermore, through transfer learning with initialized SEDNet pre-trained weights, termed SEDNetX, a performance increase is observed. The dice and Hausdorff scores recorded are 0.9336, 0.9478, 0.9061, 0.6983, 1.2691, and 0.7711 for NTC, ED, and ET, respectively. With about 1.3 million parameters and impressive performance in comparison to the state-of-the-art, SEDNet(X) is shown to be computationally efficient for real-time clinical diagnosis.

1. Introduction

A brain tumor establishes the onset of abnormality in the brain. Whether benign or malignant, tumors can proliferate to the surrounding brain tissue [1] which makes any type of tumor dangerous. A benign tumor grows slowly,

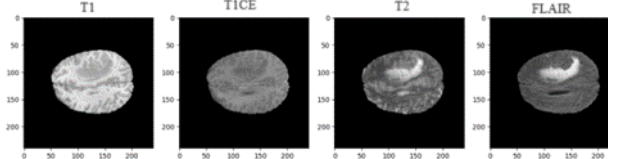


Figure 1: All modalities of a sample MRI brain tumor images of BraTS2020. The irregular, unclear, and discontinuous boundaries of tumors¹ are some of the challenges of computational tumor segmentation.

whereas, malignant tumors have the tendency to expand suddenly with some aggressiveness [2]. Gliomas constitute about 49.1% of all diagnosed malignant tumors [3], of which glioblastoma is the most common and fatal of them, with a median survival of 12 to 15 months [4]. Therefore, analysis that lends itself to identifying, isolating, and quantifying subregions of the brain with tumors is necessary for early diagnosis of cancer for planning effective treatment strategies and patient survival.

During pre-operative monitoring and assessment of brain tumors using MRI, a long-standing and widely used standard of neuro-oncology imaging [5], the neuroradiologist offers diagnosis based on the structural characteristics, enhancement patterns, and the amount of surrounding edema [6]. Despite the superior information on tumors that the MRI reveals, its interpretation and resulting diagnosis is, yet, based on the experiences and sometimes assumptions of the neuroradiologist, which is highly prone to cognitive bias [7]. In fact, the discrepancy in neuroradiologist interpretations has been quantified to account for about 60–80% of missed intracranial neoplastic abnormality and 20–40% of misinterpretation of intracranial neoplastic abnormality [8]. To bridge this diagnostic gap, research has in the past decades been geared towards the computational diagnosis of brain tumors for accurate and timely diagnosis.

Computational models can characterize complex systems due to their underlying mathematical principle, and so are better at minimizing any cognitive bias that may exist in diagnosis. Tumors can take on varying sizes, appearance, shapes, and locations [9, 10], with irregular, unclear, and discontinuous boundaries due to their heterogeneous nature and imaging artifacts as evident in Fig. 1. With computational models, irrespective of the

boundary discontinuities of tumors (even for the same patient), monitoring and assessment of tumors can be expedited and consistent and can help neuroradiologist quantify tumor progression and treatment response [11]. However, the performance, reliability, and efficiency of computational models in real-time under clinical application scenarios are dependent on several factors, 1) computational complexity, 2) validity and usefulness in clinical diagnosis, 3) ability to answer clinical and radiological challenges as mentioned by Dr. Sofie Van Cauter neuroradiologist¹. In the bid to address any of these impending factors on the applicability of computational models in real-world clinical settings for the diagnosis of brain tumors, efforts have been made by several researchers toward developing computational models for tumor analysis [12-16]. Localizing and predicting the grades of tumor [12] to minimize the time constraints of biopsy and manual inspection, understanding patterns and characteristics of tumor progression [13, 14], predicting survival [15], and/or estimating the size of a tumor [16] are all essential tasks of tumor analysis for providing patients with effective therapeutic management and treatment strategies. However, most of these tasks require that the subregions of the brain where tumors exist have been extracted. This necessitates the emphasis of the paper on the task of segmentation.

Convolutional neural networks (CNNs) are increasingly advancing brain tumor segmentation research due to their efficient capability to discover patterns in images and strong generalizability to similar patterns in unseen images. The BRATS dataset is a complex volumetric data series (2012 – 2023) having numerous slices per patient and multiple image planes (axial, coronal, and sagittal). Researchers have approached the segmentation of brain tumors with the BRATS data series from several perspectives. However, despite the research efforts in brain tumor segmentation, of which several models have been developed, some of which are [17, 18, 19, 20, 21], it is evident from the literature that the performance and efficiency of the models under clinical application scenarios are limited. This is because the computational complexity of the models is still at an all-time high, which invariably affects their validity and usefulness in clinical diagnosis. Therefore, this paper proposes a shallow encoder and decoder network named SEDNet for brain tumor segmentation. The proposed network is adapted from U-Net structure and designed to consist of sufficient hierarchical convolutional blocks in the encoding pathway capable of learning the intrinsic features of brain tumors in brain slices, and a decoding pathway with a selective skip path sufficient for capturing miniature local-level spatial features alongside the global-level features of brain tumor.

This network was specifically inspired by the localized nature of brain tumors in brain images. Though brain tumors do not assume a complex structure like the task the traditional U-Net was designed for, the high variance in appearance, and shape of tumors, coupled with the ambiguity of tumor boundaries makes it a compelling complex task that needs to be solved. Along with SEDNet, several other significant contributions of this paper are as follows:

- A robust 2D shallow encoder and decoder network (SEDNet) that uses sufficient hierarchical convolutional blocks for the encoding pathway and selective skip paths for the decoding pathway to address computational complexity while simultaneously achieving impressive tumor segmentation accuracy.
- A substantially effective preprocessing algorithm for minimizing signal randomness or proportion of noise to signal of feature maps introduced by MRI slices containing images of a brain with a corresponding empty mask.
- Priority weighted binary cross entropy (BCE) loss, and soft dice loss (WBCESD^p) proposed as an effective approach for learning optimization. This is to address the effect of class imbalance and tumor boundary irregularity while improving learning and minimizing premature model convergence.
- Initialize a SEDNet pre-trained weight, termed SEDNetX, for BraTS data series and show that data volume does not limit transfer learning when data is highly specific to a given task with minimal randomness and transferred for the same task.

The rest of this paper is organized as follows. The review of related work and the proposed system are presented in Section 2 and Section 3, respectively. Section 4 demonstrates the experimental settings, experiments, results, and discussions, while the conclusion is provided in Section 5.

2. Related work

U-Net [22] has become the state-of-the-art architecture for brain tumor segmentation. Its success in biological image segmentation has prompted numerous 2D U-Net and 3D U-Net variants for tumor segmentation [17-20]. However, the number of trainable parameters of the existing 2D U-Net and 3D U-Net architectures suggests that computational cost is still at an all-time high. For this reason, other researchers approached this problem from the perspective of a lightweight 2D U-Net. Sun and Wang [21] proposed a compact U-Net-based CNN architecture. The compactness was achieved by adopting dual convolutional layers at the encoding pathway - depthwise separable

¹ <https://healthcare-in-europe.com/en/news/challenges-in-brain-tumour-segmentation.html>

convolution and conventional convolution with reduced filter depth - a minimum of 23 and a maximum of 25. These are concatenated to continue the chain of encoding. The depthwise separable convolution as proposed by [23] is channel-based and basically for minimizing computational complexity. The decoding pathway of the architecture was designed with conventional convolution blocks and of the same filter depths, all set to 28. Other unique components of their architecture are the use of bilinear interpolation, full rectified linear unit (ReLU) designed to minimize loss of useful information, and instance normalization. Their architecture utilized only 20,308 trainable parameters and achieved dice scores of 0.772, 0.892, and 0.793, for ET, whole tumor (WT), and ED, respectively. One limitation observed is that the small filter depth in relation to the network input (168x200x4) can result in information loss. Additionally, the performance of the architecture was greatly enhanced by the post-processing steps. In [24], a shallow network was proposed. Their network contains only two convolutional blocks in the encoding and decoding pathways. They also used a convolutional filter of depth 16 for an input size of 1024x1024x1, which is not sufficient for expressing the fine-scale global information of a brain tumor. Though the network was proposed for a different task of phase retrieval, it was interesting how it utilized only 116,753 trainable parameters. Another lightweight U-Net example is the Squeeze U-Net architecture proposed in [25]. It consists of a fire module that replaces the convolutional blocks at the encoding pathway, and a transposed fire module in place of the conventional 2D transposed convolution in U-Net at the decoding pathway. The fire module consists of one convolution filter of 1x1 dimension connected to two convolution filters of 3x3 dimensions organized in parallel and their output concatenated. The same applies to the transposed fire module with a difference in transposed convolution. The squeeze U-Net reduces traditional U-Net to 2.59 million parameters.

Biological images are mostly of complex structure and the success of U-Net for segmentation of such images can be mainly attributed to the skip connection element of the U-Net architecture which allows miniature local-level spatial features to be captured alongside the global-level features, otherwise the local-level information will be immersed in the global information. The traditional U-Net was designed for a problem that maps input to the output of equal multi-level contextual information and spatial distribution, which necessitates the choice of depth and skip connections between paths. However, we argue that when the output is of single-level contextual information localized in the input map, such as presented by a brain tumor, a careful design of the skip connections becomes necessary to minimize noise and redundant features. The skip paths required are feature maps of the first two convolutional blocks for preserving the fine local-level

features and fine global-level features of a brain tumor. In this way, redundancy in the decoding computations can be minimized. This invariably reduces the number of parameters and computational efforts of the U-Net architecture for brain tumor segmentation.

3. Methodology

3.1. Proposed system

The proposed system is designed to include a preprocessor to enable more tumor signals than noise to be captured, a robust segmentation architecture, SEDNet, to minimize the computational cost of tumor segmentation while simultaneously increasing segmentation performance, and a robust optimization function to minimize the effect of class imbalance and tumor boundary irregularity on performance.

3.2. Preprocessing

The MRI slices mostly contain images of a brain with a corresponding empty mask, which can introduce some randomness or increase the proportion of noise to the signal of feature maps during training. Therefore, to ensure the proposed network focuses on learning brain slices with corresponding tumor signals, a preprocessing pipeline is proposed. This is on the argument that when the network learns the salient features that best describe the tumor structure, shape, and low-level information, it will be capable of generating feature maps of rich tumor representation for discriminating between tumor and non-tumor features. There are three phases to the proposed preprocessing pipeline, which are presented in Algorithm 1. The first phase is focused on identifying and discarding slices of a brain with no corresponding tumor mask. It determines the maximum of each mask to slice and if it is zero, the corresponding mask is considered empty and gets discarded. Then, it applies morphological operations to the non-empty mask to compute the area of the tumor in the mask, if below a threshold, then it is likely not a tumor. The second phase retrieves the count of the number of slices for each sample, that is, patients enrolled in a BraTS series, and outputs the least count. The third phase uses the output of the second phase as a threshold for retaining the final data points of a sample, such that the data points for each sample remain the same. Unlike commonly practiced in literature, the brain slices were not corrected for brightness and contrast. However, each brain slice was normalized to the range of values between 0 and 1, while the labels in each mask were converted to binary labels. Then, the NTC, ED, and ET were retrieved and combined as a three-channel image.

Algorithm 1:

INPUT: FLAIR slices per sample //original 155 slices per sample
OUTPUT: non-empty, tumor slices per sample

-----**Phase I-----**

//Remove empty and tumor less points slices
 $k \leftarrow (\text{open, close})$ //kernels for open and close
 $r \leftarrow []$
for f in sample **do**
 for i in image list **do**
 i = resize image i
 m = morphologyopen(i, k)
 m = morphologyclose(m, k, repeat)
 x \leftarrow find maximum of m
 if x == 0 **then**
 r \leftarrow create list //add files to list
 else
 c \leftarrow find Contours
 a = compute area of c
 if a $\leq T$ **then** //T, threshold for non-tumor area
 r \leftarrow create list / add more files to list
 end if
 end if
 end for
end for
//Remove files
for j in r **do**
 remove j
end for

-----**Phase II-----**

//find the number of slices per sample
 $L \leftarrow []$
for f in sample **do**
 total \leftarrow get length of f
 L \leftarrow set num
end for
least num = find minimum of L //find the minimum

-----**Phase III-----**

//let number of slices be set to the least slices of all samples
images = []
masks = []
count \leftarrow 0
for f sample **do**
 file \leftarrow set slices path
 count \leftarrow increment by 1
 if count > least num **do**
 image = get name from image list
 mask = get name from mask list
 remove image
 remove mask
 end if
end for

3.3. SEDNet and Objective Function

SEDNet is designed for segmenting tumor regions of the brain. The architecture is schematically shown in Fig. 2. The proposed network is an adapted U-Net structure that assumes a localized region in an image of a brain, though not of a complex structure like the task the traditional U-Net was designed, yet not trivial due to the high variance in appearance and shape of tumors, coupled with the ambiguity of tumor boundaries. The proposed network is designed to consist of a hierarchical encoding pathway that can learn the intrinsic features of brain tumor in brain slices, and a decoding pathway with selective skip path sufficient for capturing miniature local-level spatial features alongside the global-level features of brain tumor. The goal of SEDNet is to reduce parameters and computation for validity and usefulness in real-time, while

simultaneously increasing tumor segmentation performance.

3.3.1 Encoding Pathway

The encoding pathway of SEDNet is inspired by the U-Net encoder. Taking an input of MRI slices, $X \in \mathbb{R}^{W \times H \times C}$ where W is width, H is height and C is channel, respectively, the encoder extracts a hierarchical feature representation of brain tumor using three downsampling convolutional blocks with 3×3 filter dimension, reserved image dimension, and nonlinear activation function, ReLU, and 3×3 maxpooling layer. Each convolution block consists of two convolutional layers that reduce the feature maps as learning progresses with increasing filter depth to better learn the local-level and global-level spatial features of brain tumor. Then, a bottleneck convolutional block is added. It is set to twice $W \times H$ of the input map. X The resulting dimension of the feature map of the encoding pathway is $\frac{W}{4}, \frac{H}{4}, 2^8 C$

3.3.2 Decoding pathway

On the argument that the brain tumor task presents a problem whereby the single-level contextual information is localized in the input map, a selective skip path is designed. The decoding pathway comprises two upsampling convolution blocks: an upsampling layer of 2×2 filter dimensions, a convolutional layer of 2×2 filter dimensions which replaces the U-Net transposed convolution, reserved image dimension, nonlinear activation ReLU followed by a skip path. The selected skip paths are feature maps of the first two convolutional blocks concatenated to the upsampled feature maps of deeper layers to preserve fine scale local-level and global-level spatial features of the brain tumor, respectively. Each upsampling block is preceded by a convolution block, each of which comprises two convolutional layers of the same filter dimension and depth with reserved image dimension, and nonlinear activation ReLU. The resulting dimension of the feature map of the decoding pathway is $W, H, 2^5 C$. The output layer is a convolution of 1×1 filter dimension with a depth equal to the number of pixel-wise classes, and a sigmoid activation function to output a prediction, $Y \in \mathbb{R}^{W \times H \times C}$ where C is a three channel corresponding to NTC, ED, and ET.

3.3.3 Transfer Learning with SEDNet

Unlike the popular opinion of transfer learning in literature using models trained with substantial amounts of data, in millions, and of distinct class labels as pretrained weights, this paper theorizes that *data volume does not limit transfer learning when data is highly specific to a given task with minimal randomness and transferred for the same task*. Therefore, this paper further utilizes the saved weights of SEDNet from initial learning, pre-trained, on tumor samples for transfer learning. The learned weights were initialized as a backbone for capturing the semantics of tumor regions. Then, the layers of SEDNet

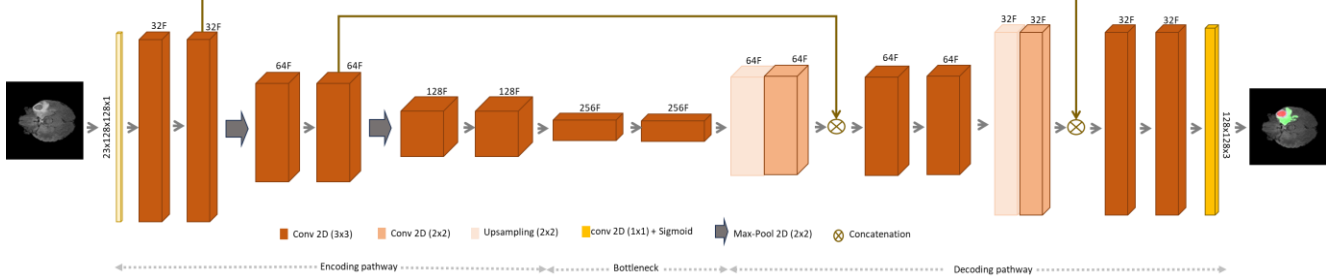


Figure 2: The proposed architecture of 2D SEDNet.

architecture was frozen, while the classification layer, was used as a feature extraction and learning mechanism to yield a prediction, $Y_T \in \mathbb{R}^{W \times H \times C}$, where Y_T , is the output of transfer learning. By this the SEDNet becomes SEDNetX. Transfer learning is highly significant to tumor segmentation because it expands the possibilities of application across the BraTS series since they share similar features. Thus, SEDNetX serves as pretrained weights for any of the BraTS series dataset.

3.3.4 Objective Function

Since tumors take on irregular, unclear and discontinuous boundaries due to their heterogeneous nature coupled with imaging artifacts due to different imaging sources, it is therefore appropriate to choose a loss function that can achieve a good performance. However, with consideration of the high-class imbalance of tumors of the BraTS series which can affect a good loss function as well as inhibit the performance of a well-achieving deep learning model [26], considerations of the type of loss function are necessary. Therefore, an experiment is needed to determine the most appropriate combination of BCE, L , and SD, S . The combinations considered are the binary cross entropy loss combined with soft dice loss (BCESD), equally weighted binary cross entropy loss combined with soft dice loss (WBCESD^e), priority weighted binary cross entropy loss combined with soft dice loss (WBCESD^p). The BCE is chosen to alleviate the class imbalance problem and the SD is preferred for computing the overlap between predicted ground truth labels with a bit of softness to accommodate near boundary labels resulting from tumor irregularity and discontinuity. The BSC and SD are mathematically expressed in Eq. 1 and Eq. 2, respectively.

$$L(Y_T, g) = \frac{1}{N} \sum_{i,j}^N \left[g_{i,j} \left(\log(Y_{T,i,j}) \right) + (1 - g_{i,j}) \cdot \left(\log(1 - Y_{T,i,j}) \right) \right] \quad (1)$$

$$S(Y_T, g) = -\frac{1}{N} \sum_{i,j}^N \left(\frac{2 \times \sum_{i,j}^N Y_{T,i,j} * g_{i,j} + \epsilon}{\sum_{i,j}^N (Y_{T,i,j} * g_{i,j}) + \sum_{i,j}^N (Y_{T,i,j} * g_{i,j}) + \epsilon} \right) \quad (2)$$

where $p_{i,j}$ is the predicted label and $g_{i,j}$ is the ground truth label at the i^{th}, j^{th} point of p and g and if a perfect match the points will correspond to a 1, otherwise, it is a 0. Usually, ϵ is added to overcome division by zero error during computation.

The objective function for the proposed SEDNet architecture is their combination (Eq. 1 and Eq. 2), which is expressed as:

$$O(Y_T, g) = L(Y_T, g) + S(Y_T, g) \quad (3)$$

$$O^e(Y_T, g) = w_a^e * L(Y_T, g) + w_b^e S(Y_T, g) \quad (4)$$

$$O^p(Y_T, g) = w_a^p * L(Y_T, g) + w_b^p S(Y_T, g) \quad (5)$$

where $w_{a,b}^e$ and $w_{a,b}^p$ are equal and prioritization weights. With $w_{a,b}^p$, more weight is given to L than S on the assumption that the class imbalance problem grossly affects the optimization function, $O^{(e,p)}$, more than tumor boundary irregularity does. Therefore, it is expected to perform better than the other combination of BCE and SD.

4. Experimental settings and results

4.1. Experimental settings

4.1.1 Data

The dataset is a part of the MICCAI conference brain tumor segmentation challenge, BraTS2020. The dataset contains four tumor modalities, T1, T1-gad, T2, and FLAIR, which were manually segmented to generate the ground truth label corresponding to the whole tumor, (WT), NTC, ED, and ET, using the same labeling protocol [27]. However, only the NTC, ED, and ET are the relevant segmentation classes in this paper. The slices are preprocessed by co-registering them to the same anatomical template and interpolating them to 1mm³ isotropic resolution, and then skull stripping them. The subsets of the data publicly available are the training and validation datasets, which contain 369 and 125 cases, respectively, though no ground truth label is available for the validation set.

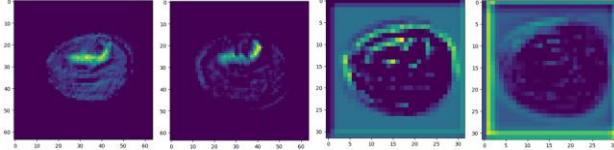


Figure 3: Information from convolution blocks of the encoding pathway of SEDNet. The samples represent the output of the first, second, third and bottleneck convolution blocks which are filter depths of 32, 64, 128, and 256.

4.1.2 Experimental parameters

The FLAIR modality encompasses all the tumor classes, as can be observed in Fig. 1, which means it is sufficient for learning the features of a tumor. Consequently, the noise and the computational cost of using all four modalities can be minimized. By applying the preprocessing algorithm on the axial plane of the 3D MRI BraTS2020 dataset, the size of each slice changes from $155 \times 240 \times 240 \times 4$ to $23 \times 128 \times 128 \times 1$, where 155 and 23 are the number of slices, 240 and 128 are the width and height of each slice, while 4 and 1 represent the modalities. This paper only utilized a single modality, the flair. The input to the network is a batch of 23 slices for each sample. Since only the training set contains ground truth labels, it was split into three – training, validation, and testing sets in the ratio 80:10:10. Then, the validation set was used for the purpose of testing for generalization. For training, the proposed SEDNet, uses the proposed loss function with ADAM optimizer and an initial learning rate of 0.0003. The adaptive learning rate was adopted and configured to gradually decrease the learning rate with a shrinkage factor of 0.3 when no improvement in the validation loss is recorded within 2 epochs. The SEDNet was trained for 50 epochs for generating weights fed into SEDNetX, retrained for 30 epochs under the same settings.

4.1.3 Evaluation Metric

Given the ground truth label and predicted label, the validity of the proposed model pixel-wise classification of a tumor based on their classes can be measured using the dice similarity coefficient (DSC), Z , and the symmetric Hausdorff distance (HD) [28], H , are computed as:

$$Z(Y_T, g) = \frac{2 \times \sum_{i,j}^N |Y_{T,i,j} * g_{i,j}| + \epsilon}{\sum_{i,j}^N (Y_{T,i,j}^2 + g_{i,j}^2) + \epsilon} \quad (6)$$

$$H(Y_T, g) = \max\{\tilde{H}(Y_T, g), \tilde{H}(g, Y_T)\} \quad (7)$$

where \tilde{H} is given as $\{min_{n \in \mathcal{G}}\{\|m, n\|\}\}$, and where $\|\cdot, \cdot\|$ is the Euclidean distance function.

Since brain tumor takes on varying sizes, appearance, shape, [9,10], with irregular, unclear and discontinuous boundaries it becomes necessary to exploit metrics capable of handling these uncertainties, and literature shows that

the DSC and HD are examples of such metrics. The DSC measures the overlap between, p and g , pixels belonging to the tumor and inclusive of those pixels at the boundary, while HD is the maximum degree of mismatch between them [28]. A higher DSC score and lower HD translate to a perfect match.

4.1.4 Implementation Resource

The Tensorflow-based deep learning library, Keras, was used in a Microsoft OS environment hosting NVIDIA’s Geforce RTX 3070 (16 GB RAM), Tensorflow-gpu 2.10.0, CUDA v11.6, and cuDNN v8.4.0.

4.2. Results and discussion

From the experiments, it is evident that even with minimal parameters and computational cost, high pixel-wise classification performances were achieved with SEDNet as demonstrated in Fig. 4 (a) and (b), Fig. 5, Fig. 6, and 7, and in Table 1, Table 2, and Table 3.

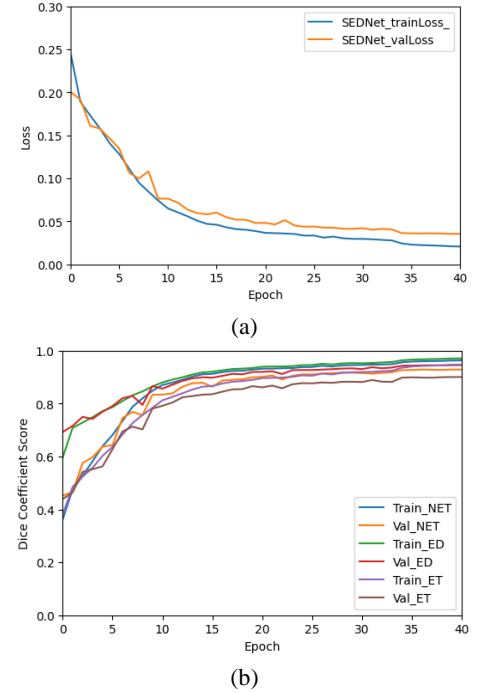


Fig 4: Training loss and accuracy per epoch for SEDNet (a) shows loss per epoch and (b) shows accuracy per epoch.

Table 1: Performance analysis of combinations of BCE and SD loss functions in the proposed segmentation system on the BraTS2020 dataset

Loss Function	Dice		
	NTC	ED	ET
BCE	0.9143	0.9376	0.8592
BCED	0.9279	0.9432	0.9001
BCESD	0.9315	0.9432	0.9014
WBCESD ^e	0.9272	0.9451	0.8875
WBCESD ^p	0.9308	0.9451	0.9026

An interesting observation can be seen in Fig. 4 (a) and (b) which show curves for SEDNet training and validation loss, and dice coefficient scores at training and validation for NTC, ED, and ET, respectively. Most loss curves on brain tumor pixel-wise classification in the literature show massive oscillations. This might signify that there exist some randomness or noisy signals in the feature maps, or that the skip connections from the deeper levels of the encoding pathway were introducing noise to the signals upsampled. The SEDNet, on the contrary, showed smooth curves from the first epoch to the 40th epoch. As can be observed, an increase in epoch decreases the training and validation loss and increases the dice scores. Therefore, it is relevant to state that the proposed system 1) sufficiently minimized the proportion of noise to signal of feature maps through the preprocessing pipeline and 2) the selective skip path was sufficient for capturing miniature local-level spatial features alongside the global-level features necessary for achieving tumor segmentation success at reduced parameters and computation cost.

To appreciate the contribution of the proposed combination of the BCE and SD, as the optimization function in the proposed system, several experiments were carried out and reported in Table 1. It included experiments with BCESD, WBCESD^e, WBCESD^p, and other loss functions such as the binary cross entropy loss (BCE) and binary cross entropy loss combined with dice loss (BCED). The experiment was necessary for determining the combination of BCE and SD that best optimizes learning and converges to a global minimum. As can be observed, WBCESD^p impacted so much on SEDNet's ability to address class imbalance and tumor boundary irregularities. The WBCESD^p loss function was observed to have better convergence performance without massive oscillations. In comparison to other loss functions experimented, WBCESD^p achieved a 0.9308 dice score for NCT, which is an increase of 0.165%, 0.29%, and 0.36%, for BCE, BCED, WBCESD^e, respectively, but a decrease of 0.07% for BCESD. Then, a dice score of 0.9451 which is an increase of 0.75%, 0.19%, 0.19%, and 0.00% for BCE, BCED, BCESD, and WBCESD^e, individually. For ET, a score of 0.9026 can be observed which is an increase of 4.34%, 0.25%, 0.12%, and 1.51% for BCE, BCED, BCESD, and WBCESD^e, respectively. Generally, these results confirm that SEDNet achieves impressive performance irrespective of the loss function. However, the WBCESD^p stood out and therefore was chosen as the loss function for the proposed segmentation system. Therefore, based on the experimental results of WBCESD^p, it can be theorized that class imbalance indeed grossly affects the optimization function, $O^{(e,p)}$, more than tumor boundary irregularities do. This is based on WBCESD^p performance compared to the other combinations.

The impressive performance of SEDNet is further

elaborated in Table 2 where the dice scores and Hausdorff scores are presented. As can be observed, the dice coefficient scores at training and validation for NTC, ED, and ET are closely related and surprisingly, they performed equivalently when evaluated on the unseen test set. Unlike the Hausdorff distance score recorded for NTC, ED, and ET in literature which are mostly in the interval (2,35), that is, $\{H|2 < H < 35\}$, SEDNet achieved minimal Hausdorff distances in the interval (0.5,1.29). The intriguing part of this score is that it extends to the unseen percentage of the BraTS2020 reserved for testing the generalizability of the model on similar samples. Interestingly, the SEDNet dice score also supersedes state-of-the-art scores which are usually on average in the interval (0.7,0.8), that is, $\{Z|0.7 < Z < 0.8\}$. It achieved dice scores in the interval (0.90,0.97) expressed as: $\{Z|0.90 < Z < 0.97\}$. These results further show that the proposed system, which encompasses an efficient preprocessing pipeline and a robust SEDNet architecture impacted by the selective skip path, is significant to brain tumor segmentation.

On the BraTS2020 set designated for testing, SEDNetX can be observed in Table 2 to advance the dice score performance of SEDNet by 0.28%, 0.27%, 0.35% for NTC, ED, and ET, respectively. The interval is in the range (0.90,0.97) which takes the form, $\{Z|0.90 < Z < 0.97\}$. The substantial gain in performance that is observed with SEDNetX shows that transfer learning can be achieved in a contrary fashion than it has long been understood and presented in the literature. In essence, it means that data volume in millions and of distinct class labels are not more important than highly specific data of a given task with minimal randomness and transferred for the same task. With regard to Hausdorff distance, SEDNetX achieved scores in the interval (0.5,1.28), expressed as $\{H|0.5 < H < 1.28\}$ across training, validation, and testing set scores recorded for NTC, ED, and ET.

Since SEDNetX improved the performance of SEDNet, it became the basis for visual evaluation. Fig. 5 (a) and (b) depict the visual results of SEDNetX in comparison with the ground truth (GT) labels. Precisely, Fig. 5 (a), shows that the predicted tumors were a close match to the GT tumors. On the contrary, small-resolution tumors, that is, miniaturized tumors, challenged the performance of SEDNetX as can be seen in Fig. 5 (b). However, some of these examples can be categorized as not tumors but were possibly missed by the preprocessing algorithm. Similar performance can be seen in Fig. 7 where the performance of SEDNetX was demonstrated on the BraTS2021 dataset. On the validation set, as shown in Fig. 6, the segmentation results appear to be a close replica of the tumor region shown in the sampled MRI slices.

5. Conclusion

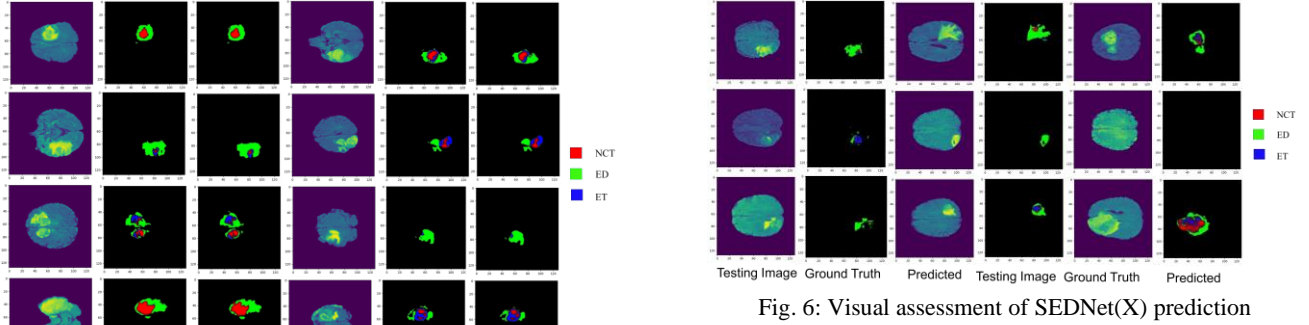
This paper proposed a tumor segmentation system that

Table 2: Performance comparison of state-of-the-art and SEDNet(X) on the BraTS2020 dataset.

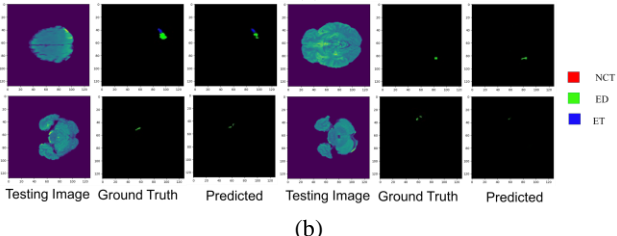
Model	Data set	Dice			Hausdorff			Training Parameters
		NTC	ED	ET	NTC	ED	ET	
dResU-Net [17]	Testing	0.8357	-	0.8004	-	-	-	30.47 million
SA-Net [18]	Testing	0.8433	-	0.8177	17.9697	-	13.4298	16.5 million
Lightweight [19]	Testing	0.9460	-	0.8860	9.2420	-	3.4640	7.5 million
SEDNet	Training	0.9641	0.9721	0.9493	0.5842	0.9952	0.6219	1.3 million
SEDNet	Validation	0.9287	0.9454	0.9004	0.7184	1.2967	0.7786	
SEDNet	Testing	0.9308	0.9451	0.9026	0.7040	1.2866	0.7762	
SEDNetX	Training	0.9701	0.9780	0.9588	0.5455	0.9087	0.5747	
SEDNetX	Validation	0.9314	0.9483	0.9048	0.7122	1.2800	0.7716	
SEDNetX	Testing	0.9336	0.9478	0.9061	0.6983	1.2691	0.7711	

Table 3: Qualitative evaluation of SEDNetX on BraTS2021 dataset.

Model	Data set	Dice			Hausdorff		
		NTC	ED	ET	NTC	ED	ET
SEDNetX	Training	0.9277	0.9820	0.9622	0.6610	0.9156	0.5831
SEDNetX	Validation	0.8845	0.9583	0.9039	0.8275	1.2165	0.8007
SEDNetX	Testing	0.8967	0.9591	0.9064	0.8334	1.2485	0.8242



(a)



(b)

Figure 5: Visual evaluation of SEDNet(X) on BraTS2020. (a) show that SEDNet(X) prediction results were a close match to GT and (b) illustrate that small-resolution tumors were not well captured by SEDNet(X).

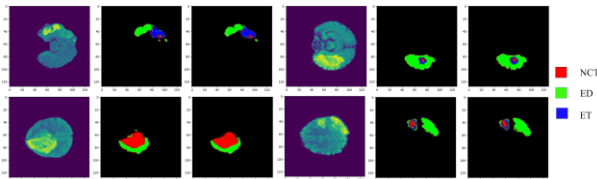


Figure 7: Visual evaluation of SEDNet(X) segmentation performance on the BraTS2021 dataset.

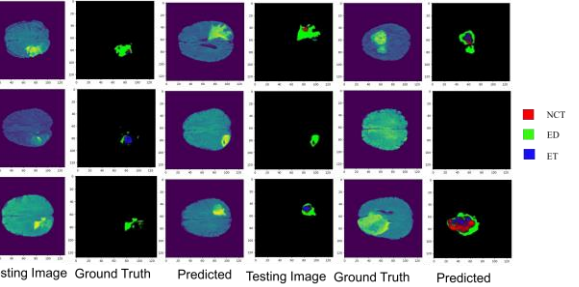


Fig. 6: Visual assessment of SEDNet(X) prediction performance on BraTS2020 validation set.

comprises a shallow encoder-decoder network named SEDNet, a preprocessor, and an optimization function. SEDNet architecture design included sufficient hierarchical convolution blocks in the encoding and decoding pathways with selective skip paths. Through the transfer learning with initialized SEDNet pre-trained weights, SEDNetX was born. SEDNet(X) on the BraTS2020 dataset achieved dice and Hausdorff scores of 0.9336, 0.9478, 0.9061, and 0.6983, 1.2691, 0.7711 for NTC, ED, and ET, respectively. With about 1.3 million parameters and impressive performance in comparison to the state-of-the-art, SEDNet(X) is computationally efficient for real-time clinical diagnosis. While (1) and (2) of the impending factors that necessitate application of computational models to tumor analysis have been addressed in this paper, (3) is still outstanding, and therefore future work will include efforts to utilize the model to answer clinical and neuroradiological challenges. Additionally, since most of the instances where SEDNet(X) results vary from the GT were likely not tumors, a neuroradiologist analysis for defining non-tumor slices is necessary.

References

[1] Fidan Seker-Polat, Pinarbasi Degirmenci, Ihsan Solaroglu, and Tugba Bagci-Onder. Tumor cell infiltration into the brain in glioblastoma: from mechanisms to clinical perspectives. *Cancers* 14(2): pages 443, 2022.

[2] Padmini Bisoyi. A brief tour guide to cancer disease. *Understanding cancer*, Academic Press, pages 1-20, 2022.

[3] Quinn Ostrom, Gino Cioffi, Kristin Waite, Carol Kruchko, and Jill Barnholtz-Sloan. CBTRUS statistical report: primary brain and other central nervous system tumors diagnosed in the United States in 2014–2018. *Neuro-oncology* 23(3), pages iii1-iii105, 2021.

[4] Andrew Norden, Jan Drappatz, and Patrick Wen. Novel anti-angiogenic therapies for malignant gliomas. *The Lancet Neurology*, 7(12), pages 1152-1160, 2008.

[5] Javier Villanueva-Meyer, Marc C. Mabray, and Soonmee Cha. Current clinical brain tumor imaging. *Neurosurgery* 81(3), page 397, 2017.

[6] Richard Schwartz. Neuroradiology of brain tumors. *Neurologic clinics*,13(4), pages 723-756, 1994.

[7] Jason Itri and Sohil Patel. Heuristics and cognitive error in medical imaging. *American Journal of Roentgenology*, 210(5), pages 1097-1105, 2018.

[8] Michael Bruno, Eric Walker, and Hani Abujudeh. Understanding and confronting our mistakes: the epidemiology of error in radiology and strategies for error reduction. *Radiographics*, 35(6), pages 1668-1676, 2015.

[9] Marriam Nawaz, Tahira Nazir, Momina Masood, Awais Mehmood, Rabbia Mahum, Muhammad Attique Khan, Seifedine Kadry, and Orawit Thinnukool. Analysis of brain MRI images using improved cornernet approach. *Diagnostics*, 11(10), pages 1856, 2021.

[10] Ujjwal Baid, Sanjay Talbar, Swapnil Rane, Sudeep Gupta, Meenakshi H. Thakur, Aliasgar Moiyadi, Nilesh Sable, Mayuresh Akolkar, and Abhishek Mahajan. A novel approach for fully automatic intra-tumor segmentation with 3D U-Net architecture for gliomas. *Frontiers in computational neuroscience*, 14 (2020), page 10, 2020.

[11] Zeynettin Akkus, Alfia Galimzianova, Assaf Hoogi, Daniel L. Rubin, and Bradley J. Erickson. Deep learning for brain MRI segmentation: state of the art and future directions. *Journal of digital imaging* 30 (2017), pages 449-459, 2017.

[12] Fatima Zulfiqar, Usama Ijaz Bajwa, and Yasar Mehmood. Multi-class classification of brain tumor types from MR images using EfficientNets. *Biomedical Signal Processing and Control*, 84 (2023), page 104777, 2023.

[13] Deqi Zhou, Loc Tran, Jihong Wang, and Jiang Li. A comparative study of two prediction models for brain tumor progression. *In Image Processing: Algorithms and Systems XIII*, 9399, pages 257-263, 2015.

[14] Cameron Meaney, Sunit Das, Errol Colak, and Mohammad Kohandel. Deep learning characterization of brain tumours with diffusion weighted imaging. *Journal of Theoretical Biology*, 557 (2023), page 111342, 2023.

[15] Li Sun, Songtao Zhang, Hang Chen, and Lin Luo. Brain tumor segmentation and survival prediction using multimodal MRI scans with deep learning. *Frontiers in neuroscience*, 13 (2019), page 810, 2019.

[16] Ivan Ezhov, Jana Lipkova, Suprosanna Shit, Florian Kofler, Nore Collomb, Benjamin Lemasson, Emmanuel Barbier, and Bjoern Menze. Neural parameters estimation for brain tumor growth modeling. In *Medical Image Computing and Computer Assisted Intervention–MICCAI 2019: Proceedings of the 22nd International Conference, Shenzhen, China, Part II* 22, pages 787-795, 2019.

[17] Rehan Raza, Usama Ijaz Bajwa, Yasar Mehmood, Muhammad Waqas Anwar, and M. Hassan Jamal. dResU-Net: 3D deep residual U-Net based brain tumor segmentation from multimodal MRI. *Biomedical Signal Processing and Control*, 79 (2023), page 103861, 2023.

[18] Yuan, Yading. Automatic brain tumor segmentation with scale attention network. In *Brainlesion: Glioma, Multiple Sclerosis, Stroke and Traumatic Brain Injuries: 6th International Workshop, BrainLes 2020, Held in Conjunction with MICCAI 2020, Lima, Peru, Part I* 6, pages 285-294, 2021.

[19] Keerati Kaewrak, John Soraghan, Gaetano Di Caterina, and Derek Grose. Modified U-Net for automatic brain tumor regions segmentation. In *Proceedings of IEEE 27th European Signal Processing Conference* pages 1-5, 2019.

[20] Tomasz Tarasiewicz, Michal Kawulok, and Jakub Nalepa. Lightweight u-nets for brain tumor segmentation. In *Brainlesion: Glioma, Multiple Sclerosis, Stroke and Traumatic Brain Injuries: 6th International Workshop, BrainLes 2020, Held in Conjunction with MICCAI 2020, Lima, Peru, Part II* 6, pp. 3-14, 2020.

[21] Yanming Sun, and Chunyan Wang. A computation-efficient CNN system for high-quality brain tumor segmentation, *Biomedical Signal Processing and Control*, 74 (2022), page 103475, 2022.

[22] Olaf Ronneberger, Philipp Fischer, and Thomas Brox. U-Net: Convolutional networks for biomedical image segmentation. In *Proceedings of the 18th International Conference on Medical Image Computing and Computer-Assisted Intervention–MICCAI 2015*, Munich, Germany, Part III 18, pages 234-241, 2015.

[23] François Chollet. Xception: Deep learning with depthwise separable convolutions. In *Proceedings of the IEEE Conference on computer vision and pattern recognition*, pages 1251-1258, 2017.

[24] Samuel Li, Matthew French, Konstantin Pavlov, and Heyang Li. Shallow U-Net deep learning approach for phase retrieval in propagation-based phase-contrast Imaging. *Developments in X-Ray Tomography XIV*, 12242, 2022.

[25] Nazanin Beheshti, and Lennart Johnsson. Squeeze u-net: A memory and energy efficient image segmentation network. In *Proceedings of the IEEE/CVF conference on computer vision and pattern recognition workshops*, pages 364-365, 2020.

[26] Carole Sudre, Wenqi Li, Tom Vercauteren, Sébastien Ourselin, and Jorge Cardoso. Generalized dice overlap as a deep learning loss function for highly unbalanced segmentations. *Proceedings of the third International Workshop on Deep Learning in Medical Image Analysis and Multimodal Learning for Clinical Decision Support*, Québec City, QC, Canada, pages 240-248, 2017.

[27] Bjoern Menze, Andras Jakab, Stefan Bauer, Jayashree Kalpathy-Cramer, Keyvan Farahani, Justin Kirby, Yuliya Burren et al. The multimodal brain tumor image segmentation benchmark (BRATS)." *IEEE transactions on medical imaging* 34, no. 10 (2014): 1993-

[28] Abdel Taha, and Allan Hanbury. An efficient algorithm for calculating the exact Hausdorff distance. *IEEE transactions on pattern analysis and machine intelligence* 37, no. 11 (2015): 2153-2163.